Journal of Solid State Chemistry 184 (2011) 70–80

Contents lists available at ScienceDirect

Journal of Solid State Chemistry

journal homepage: www.elsevier.com/locate/jssc

Crystal-chemistry of mullite-type aluminoborates $Al_{18}B_4O_{33}$ and Al_5BO_9: A stoichiometry puzzle

Martin Fisch [a,*], Thomas Armbruster [a], Daniel Rentsch [b], Eugen Libowitzky [c], Thomas Pettke [d]

[a] Mineralogical Crystallography, Institute of Geological Sciences, University of Bern, Freiestrasse 3, CH-3012 Bern, Switzerland
[b] EMPA, Swiss Federal Laboratories for Materials Science and Research, Laboratory for Functional Polymers, Überlandstrasse 129, CH-8600 Dübendorf, Switzerland
[c] Institut für Mineralogie und Kristallographie, Universität Wien - Geozentrum, Althanstrasse 14, A-1090 Wien, Austria
[d] Rock-Water Interaction Group, Institute of Geological Sciences, University of Bern, Baltzerstrasse 1+3, CH-3012 Bern, Switzerland

ARTICLE INFO

Article history:
Received 17 August 2010
Received in revised form
21 October 2010
Accepted 26 October 2010
Available online 31 October 2010

Keywords:
Al_5BO_9
$Al_{18}B_4O_{33}$
Aluminoborate
Mullite-type structure
Boron-mullite
Crystal-chemistry

ABSTRACT

Orthorhombic Al_2O_3-rich aluminoborate is an important ceramic material for which two slightly different compositions have been assumed: Al_5BO_9 ($5Al_2O_3{:}B_2O_3$) and $Al_{18}B_4O_{33}$ ($9Al_2O_3{:}2B_2O_3$). The formula $Al_{18}B_4O_{33}$ ($=Al_{4.91}B_{1.09}O_9$) was derived from results of chemical analyses when crystal structure data were not yet available. Subsequent structural investigations indicated Al_5BO_9 composition. Nevertheless, $Al_{18}B_4O_{33}$ was still accepted as the correct stoichiometry assuming that additional B replaces 9% Al.

Powder samples of both compositions and ones with excess boron were prepared by solid state reactions between α-Al_2O_3 and B_2O_3/H_3BO_3 at temperatures above 1100 °C and single-crystals were grown from flux at 1100 and 1550 °C. Products were investigated by single-crystal and powder XRD, ^{11}B and ^{27}Al solid-state MAS-NMR, Raman and FTIR spectroscopy as well as Laser-ablation ICP-MS. No indication of the predicted 9% B→Al substitution was found. LA ICP-MS indicated 12.36(27) wt% B_2O_3 corresponding to $Al_{4.97}B_{1.03}O_9$. Hence, the suggested $Al_{18}B_4O_{33}$ stoichiometry can be excluded for all synthesized samples. A very low amount of Al vacancies at a five-fold coordinated site are likely, charge balanced by an additional nearby three-fold coordinated B site. All evidences indicate that the title compound should be reported as $Al_{5-x}B_{1+x}O_9$ with $x < 0.038(6)$, which is close to Al_5BO_9.

1. Introduction

Mullite used as ceramic raw material is an important and versatile compound in the system SiO_2–Al_2O_3. Its properties include high thermal stability, very low thermal expansion, low heat conductivity, high creep and corrosion resistance and high stiffness [1]. The composition of mullite is rather variable: $Al_2(Al_{2+2x}Si_{2-2x})O_{10-x}$, $0.2 < x < 0.5$. However, the most common compositions are 3:2 mullite, $3Al_2O_3{:}2SiO_2$, $x=0.25$ and 2:1 mullite, $2Al_2O_3{:}SiO_2$, $x=0.4$.

In the system SiO_2–Al_2O_3–B_2O_3, Werding and Schreyer [2,3] introduced the term 'boron-mullite' for compounds within a compositional range between 3:2 and 2:1 mullite and two silicon-free aluminoborate members (Fig. 1), Al_5BO_9 ($5Al_2O_3{:}B_2O_3$) with a mullite-type structure [4] and $AlBO_3$ ($Al_2O_3{:}B_2O_3$) of calcite structure-type, stable under hydrothermal high-pressure conditions [5,6]. More recently, the term mullite-type boron compound has been defined [7] for corresponding structures in the binary system Al_2O_3–B_2O_3 whereas the name boromullite [8] is reserved for a mineral with sillimanite- and Al_5BO_9-like modules. In addition, Al_3BO_6 [5] with norbergite structure-type [9] was synthesized above 25 kbar and 800 °C and rhombohedral $Al_4B_6O_{15}$ with a microporous framework consisting of AlO_6 octahedra and BO_3 units has been produced from $AlCl_3$ and H_3BO_3 at 350 °C [10].

In the Al_2O_3-rich part of the phase diagram, $Al_{18}B_4O_{33}$ ($9Al_2O_3{:}2B_2O_3$) is compositionally very close to Al_5BO_9 ($5Al_2O_3{:}B_2O_3$). This material gained industrial interest because of mullite-like properties. Due to its low-cost production ($\frac{1}{10}$ to $\frac{1}{20}$ of the cost of SiC [11,12]), its easy fabrication in large quantities [13–19], its high strength [20–22], and its low thermal expansion and conductivity [23,24] the compound is used as reinforcer in metal matrix composites [14,17]. Further applications include reinforcement in fire insulations for ships, construction components in nuclear reactors because of neutron absorbing capabilities, and in refractory linings due to high resistance against boron-rich glass melts [25 and references therein]. Recently, nanotubes have been synthesized [26,27] and aluminoborate fibers have been successfully coated by boron nitride to lower interface reactions and enhance strength between matrix and aluminoborate nanowires or whiskers [12,28,29].

Although the aluminoborate discussed above is of high importance, results of crystal-chemical investigations have remained inconsistent. This mullite-type boron compound is reported with

* Corresponding author. Fax: +41 31 631 39 96.
E-mail address: fisch@krist.unibe.ch (M. Fisch).

0022-4596/$ - see front matter © 2010 Elsevier Inc. All rights reserved.
doi:10.1016/j.jssc.2010.10.032

two slightly different stoichiometries, $Al_{18}B_4O_{33}=Al_{4.91}B_{1.09}O_9=9Al_2O_3{:}2B_2O_3$ and $Al_5BO_9=5Al_2O_3{:}B_2O_3$ (Table 1), both crystallizing in the same mullite-type structure. There are no studies to date clarifying whether both similar compounds exist, probably because applications of this material were considered to be more important than its exact chemical characterization. Persistent assumption of $Al_{18}B_4O_{33}$ stoichiometry may thus have complied with tradition as this compound was originally defined on early analytical data without considering the crystal structure.

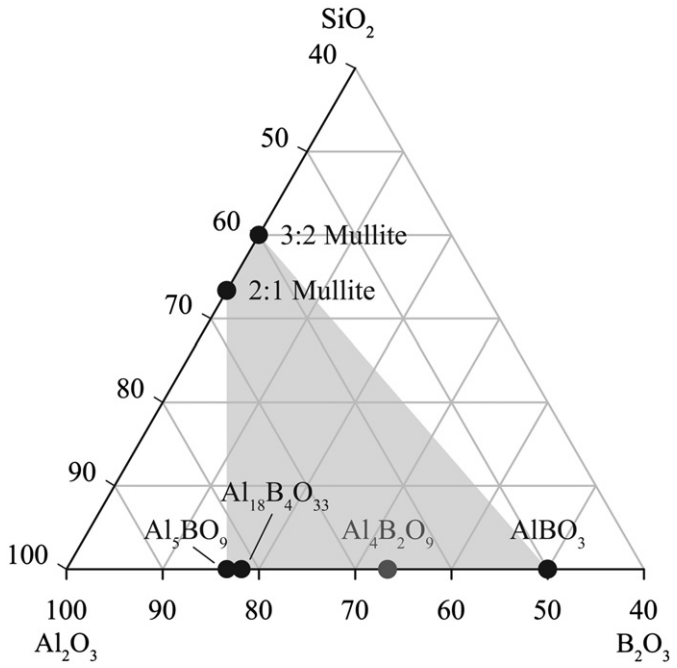

Fig. 1. Al_2O_3-rich part of the ternary system SiO_2–Al_2O_3–B_2O_3. The boron-mullite stability field according to Werding and Schreyer [2,3] is represented by the gray area. All units in mol%.

Table 1
Theoretical composition of Al_5BO_9 and $Al_{18}B_4O_{33}$.

	Al_2O_3:B_2O_3	Al_2O_3 (wt%)	B_2O_3 (wt%)	Al_2O_3 (mol%)	B_2O_3 (mol%)
Al_5BO_9	5:1	87.99	12.01	83.33	16.66
$Al_{18}B_4O_{33}$	9:2	86.83	13.17	81.81	18.18

$Al_{18}B_4O_{33}$ and Al_5BO_9 contain only trivalent cations, though of different radius. Al^{3+} and B^{3+} may both occur in four-fold coordination. Therefore, both Al and B may exist as a solid solution at a tetrahedrally coordinated site of a mullite-type structure. On the other hand, Al–O distances in an AlO_4 tetrahedron are ca. 1.75 Å [30] whereas B–O distances are ca. 1.476 Å [31]. This bond length difference of ca. 15% seems to contradict an extensive solid solution. Furthermore, it could be expected that the degree of this substitution is temperature dependent.

The aim of this study is an investigation of aluminoborate samples, produced above 1100 °C by different synthesis routes with a compositional range allowing formation of $Al_{18}B_4O_{33}$ and/or Al_5BO_9. Using single-crystal and powder X-ray diffraction, solid-state ^{11}B and ^{27}Al MAS-NMR, FTIR, Raman spectroscopy and Laser-ablation ICP-MS compositional measurements, the composition of this important compound will be clarified.

2. Historical background

In the late 19th century, Mallard [32] studied needle-like, facetted crystals with orthorhombic symmetry of supposed $3Al_2O_3{:}B_2O_3$ composition, synthesized by Ebelmen [33]. Until then, the only known aluminoborate was the mineral jeremejevite, $Al_6(BO_3)_5(F,OH)_3$ [32,34]. In 1938, Benner and Baumann [35] patented synthesis of an aluminoborate starting from molten Al_2O_3 and B_2O_3. These acicular, orthorhombic crystals were assumed to have $3Al_2O_3{:}B_2O_3$ composition. Mullite-like physical properties qualified this aluminoborate as a new ceramic raw material. Cell dimensions (Table 2) derived from powder X-ray diffraction were presented by Baumann and Moore [36]. From the density of 2.93 g/cm^3, they concluded that the correct formula of the crystals is $9Al_2O_3{:}2B_2O_3$ ($Al_{18}B_4O_{33}$), with a unit cell content of $Z=1.1$. Dietzel and Scholze [37] studied glasses in the system SiO_2–Al_2O_3–B_2O_3. From analyses of crystalline by-products they proposed a solid solution between 3:2 mullite and $Al_{18}B_4O_{33}$. Subsequent experiments in the system Al_2O_3–B_2O_3 [38] indicated a new mullite-type phase of $2Al_2O_3{:}B_2O_3$ ($Al_4B_2O_9$) composition [39,40] obtained by heating Al_2O_3 in a B_2O_3 flux at 1000 °C. According to the Al_2O_3–B_2O_3 phase diagram, $Al_4B_2O_9$ transforms to $Al_{18}B_4O_{33}$ at 1035 °C [38,41]. Sokolova et al. [4] grew aluminoborate single-crystals by cooling an Al_2O_3–B_2O_3–Y_2O_3–K_2O–MoO_3 melt from 1150 to 950 °C. Cell dimension and orthorhombic symmetry were in accordance with previous findings for $Al_{18}B_4O_{33}$. However, single-crystal X-ray structure refinement yielded Al_5BO_9 composition with $Z=4$ instead of $Al_{18}B_4O_{33}$ (Table 2). The structure was described with one AlO_6 octahedron, three AlO_4 tetrahedra and one planar BO_3 group. Results of unspecified chemical analyses yielded 14 wt% B_2O_3

Table 2
Chemical and crystallographic details of aluminoborate $9Al_2O_3{:}2B_2O_3$ from cited literature.

	Baumann and Moore [36]	Dietzel and Scholze [37]	Scholze [38]	Sokolova et al. [4]	Ihara et al. [42]	Garsche et al. [25]	Mazza et al. [39]
a-axis (Å)	15.0		5.68(5)	5.6673(7)	5.682(13)	7.6942(1)	7.621
b-axis (Å)	7.5		14.98(10)	15.011(2)	14.973(34)	15.0110(2)	7.621
c-axis (Å)	5.67		7.693(1)	7.693(1)	7.692(17)	5.6689(1)	2.833
Volume (Å^3)				654.4(2)		654.74	
Z	1.1		1.09	4	1.09	1.09	1.0
Space group	Orthorhombic		*Cmc*2$_1$, *C*2*cm*, *Cmcm*	*Cmc*2$_1$	*Cmc*2$_1$	*A*2$_1$*am*	*Pbam*
Density (g cm^3)	2.93		2.94(1)	2.96	2.93(1)		
Assigned formula	$Al_{18}B_4O_{33}$	$Al_{18}B_4O_{33}$	$Al_{18}B_4O_{33}$	Al_5BO_9	Al_5BO_9	$Al_{18}B_4O_{33}$	Al_5BO_9
B_2O_3 (wt%)		13.2	13.3	14	13.1		
Al_2O_3 (wt%)		86.6	86.7	86	86.9		
Stoichiometry from wt%		$Al_{18}B_4O_{33}$, $Al_{4.91}B_{1.09}O_9$[a]	$Al_{17.96}B_{4.04}O_{33}$, $Al_{4.90}B_{1.10}O_9$[a]	$Al_{17.77}B_{4.23}O_{33}$, $Al_{4.85}B_{1.15}O_9$[a]	$Al_{18.02}B_{3.98}O_{33}$, $Al_{4.91}B_{1.09}O_9$[a]		

[a] Normalized to 9 oxygen.

(no esd's given), which is closer to $Al_{18}B_4O_{33}$ than to Al_5BO_9 (Table 1). Single-crystals grown in the system $CaO–Al_2O_3–B_2O_3$ were also studied by Ihara et al. [42]. Results of gravimetric analyses agreed with $Al_{18}B_4O_{33}$, $Z=1.09$ (Table 2), but the structural data were in agreement with those of Sokolova et al. [4]. They concluded that two of the Al-tetrahedra specified by Sokolova et al. [4] are more precisely characterized as five-fold coordinated $Al^{(V)}$ polyhedra. The discrepancy between the crystallographically derived composition of Al_5BO_9 and the chemical composition pointing to $Al_{18}B_4O_{33}$ was explained with a disordered structure in which $\frac{1}{11} \approx 9\%$ of $Al^{(IV)}$ is substituted by tetrahedrally coordinated $B^{(IV)}$.

Garsche et al. [25] produced single-crystals by fusion of Al_2O_3 and B_2O_3 in sealed platinum capsules at 1500 °C. X-ray powder and single-crystal diffraction data (Table 2) are in agreement with findings of Solokova et al. [4] and Ihara et al. [42]. Without further investigations, the compound was reported as $Al_{18}B_4O_{33}$, based on the tetrahedral B substitution proposed by Ihara et al. [42].

The Al-coordination in '$Al_{18}B_4O_{33}$' has also been investigated by ^{27}Al MAS-NMR [43–45] on samples produced according to Garsche et al. [25]. One $Al^{(IV)}$, two distinct $Al^{(V)}$ and one $Al^{(VI)}$ site were assigned with multiplicities of 1:1:1:2 in accordance with previous crystal structure data [4,25,42].

Mazza et al. [39] synthesized crystalline products from an amorphous precursor of H_3BO_3 and $Al(NO_3)_3 \cdot 9H_2O$ and proposed a solid solution $Al_{6-x}B_xO_9$ with $1 \le x \le 3$. The structures were solved using a pseudotetragonal mullite model in space group *Pbam* (Table 2). FTIR spectra of a member with $x=1$ showed no evidence of $B^{(IV)}$, which was later also confirmed by ^{11}B MAS-NMR [46]. Mazza et al. [39] consider Al_5BO_9 as being stable in the temperature regime between 900 and 1000 °C, leading to $Al_{18}B_4O_{33}$ with space group $Cmc2_1$ upon heating at higher temperature.

3. Experimental

3.1. Sample preparation

Using stoichiometric mixtures and mixtures containing excess boron to exclude B_2O_3 as the limiting factor for $Al_{18}B_4O_{33}$ formation (due to boron evaporation at high temperature), starting materials were prepared in order to allow formation of $Al_{18}B_4O_{33}$ and/or Al_5BO_9. All syntheses were performed in lid-covered platinum crucibles in air. Three different synthesis routes were followed: (1) powder samples *b*, *c* and *e* were prepared by solid-state reactions of α-Al_2O_3 with B_2O_3 or H_3BO_3. The powders were thoroughly mixed, pressed to pellets and subsequently heated at 1100 or 1200 °C. (2) Powder sample *d* was produced from an amorphous precursor prepared with $Al(NO_3)_3 \cdot 9H_2O$ and H_3BO_3, according to [39]. The denitrified raw material was heated at 1100 °C. (3) Single-crystals were grown from a mixture of $9Al_2O_3$:$2B_2O_3$ in a K_2CO_3+$3MoO_3$ flux (borate/flux ratio ca. 1:9) by cooling the melt at 10 °C/h from 1100 to 600 °C (sample *a*) and from a pressed pellet (previously heated at 1200 °C) consisting of Al_2O_3:$3.3H_3BO_3$ in B_2O_3 flux by slow cooling (15 °C/h) from 1550 to 1250 °C (sample *f*). Fluxes were dissolved in hot deionized H_2O. Prior to further investigations, samples were washed in warm deionized H_2O to eliminate any remaining H_3BO_3 or B_2O_3. Details on samples and synthesis conditions are given in Table 3.

Both K_2CO_3+$3MoO_3$ and B_2O_3 flux methods yielded elongated single-crystals with different habits. Radially grown crystals from sample *a* were of elongate prismatic shape with a rather smooth surface but with Al_2O_3 inclusions. No inclusions were found in crystals from sample *f*, but they had a rather rough and flaky surface (Fig. 2). A sample of $Al_4B_2O_9$ [39,40] was prepared according to Fischer et al. [40] and used as reference compound for tetrahedrally coordinated $B^{(IV)}$ in FTIR, Raman and ^{11}B MAS-NMR spectroscopy.

3.2. X-ray diffraction

A full intensity dataset was measured with an Enraf Nonius CAD4 diffractometer on a single-crystal of sample *a* (Table 4). Lattice parameters were determined from 24 reflections centered at four high-angular settings with $\pm 37.9^\circ < \theta < \pm 44.4^\circ$ in order to reduce crystal and beam alignment errors. After correcting the data for Lorentz-polarization and absorption effects with WinGX v. 1.80.05 software package [47], the structure was solved by direct methods and refined with Bruker ShelXTL v. 6.10 [48] using neutral atomic scattering factors in space group $Cmc2_1$ (no. 36) with $Z=4$. The Flack parameter [49] of 0.43(10) indicated 1:1 merohedral twinning of the selected crystal.

Due to its significantly smaller size, a full intensity dataset of a crystal from sample *f* was collected with a Bruker Smart Apex2 CCD diffractometer (Table 4). Subsequently 15 reflections centered at four angular settings with $\pm 11.0^\circ < \theta < \pm 30.0^\circ$ were measured with the CAD4 for direct comparison of lattice parameters with those of sample *a*. CCD data were integrated and empirically absorption-corrected using Apex2 v. 2009-11.0 software package [50]. The structure was refined with Bruker ShelXTL v. 6.10 [48] using the structural model obtained from sample *a*. A Flack parameter of 0.60(11) indicated 1:1 merohedral twinning of the crystal. Single-crystal data collection parameters are reported in Table 4.

XRD powder patterns were measured with a PANalytical X'Pert Pro MPD diffractometer equipped with a Cu X-ray source (40 kV/40 mA) and an X'Celerator detector. Automatic divergence slits and 0.02 radian soller slits were used. Patterns were collected from 10° to 80° 2θ with a step size of 0.002° 2θ/step at 100 s/step. Lattice parameters were derived from Pawley refinements to precisely extract peak maxima by treating the data independently from the structural model. Excess Al_2O_3 (if present) was quantified by Rietveld refinements. It was not possible to estimate the amount of excess B_2O_3 or H_3BO_3 prior to the final washing step due to fast hydration of B_2O_3, resulting in a poorly crystalline mix of B_2O_3 and H_3BO_3. All powder XRD data were handled with Topas-Academic v. 4.1 [51] using the fundamental parameter approach for peak-shape modeling.

3.3. Solid-state ^{11}B and ^{27}Al MAS-NMR

^{11}B and ^{27}Al MAS-NMR spectra were recorded on a Bruker Avance 400 NMR spectrometer (9.4 T) using a 2.5 mm CP/MAS

Table 3
Starting materials, synthesis conditions and analytical methods used for sample characterization.

Sample	Al_2O_3:B_2O_3	Starting materials	Temperature	Product	Analyzed with
a	9:2	Al_2O_3, B_2O_3 in K_2CO_3+$3MoO_3$ Flux	1100 → 600 °C	Single-crystals	SX/P-XRD, MAS-NMR, LA ICP-MS
b	9:2	Al_2O_3, B_2O_3	1200 °C for 10 h	Powder	P-XRD, MAS-NMR
c	5:1	Al_2O_3, B_2O_3	1200 °C for 10 h	Powder	P-XRD, MAS-NMR
d	1:2	$Al(NO_3)_3 \cdot 9H_2O$, H_3BO_3	1100 °C for 5 h	Powder	P-XRD, MAS-NMR
e	1.2:1	Al_2O_3, H_3BO_3	1200 °C for 44 h	Powder	P-XRD, MAS-NMR, Raman, FTIR
f	1:3.3	Al_2O_3, H_3BO_3 in B_2O_3 Flux	1500 → 1250 °C	Single-crystals	SX/P-XRD, MAS-NMR, LA ICP-MS

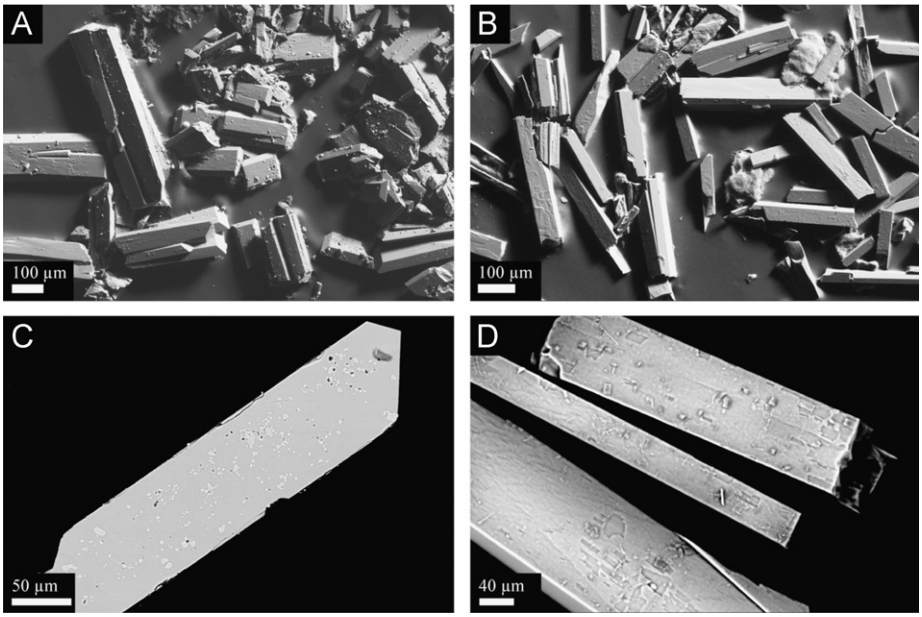

Fig. 2. SEM image of samples *a* and *f*: (A) secondary electron (SE) picture of sample *a* showing the prismatic habit of the crystals. (B) SE picture showing the elongate prismatic crystals from sample *f*. (C) Back scattered electron (BSE) image of Al_2O_3 inclusions as bright dots in a polished crystal of sample *a*. (D) BSE image showing the rough and flaky surface of crystals from sample *f*.

Table 4
Measurement setup, indexing and refinement parameters for single-crystal X-ray diffraction data collection and structure refinement of samples *a* and *f*. Note that lattice parameters can only be compared from measurements performed on the CAD4 diffractometer.

	Sample *a*	Sample *f*
Measurement type	Full intensity dataset	Full intensity dataset
Diffractometer	Enraf Nonius CAD4	Bruker Smart APEX2 CCD
X-ray radiation	Mo*K*α (0.71073 Å)	Mo*K*α (0.71073 Å)
X-ray power	50 kV, 40 mA	50 kV, 40 mA
Crystal size	0.2 × 0.13 × 0.05 mm^3	0.15 × 0.025 × 0.05 mm^3
Measurement time	Max. 120 s/step	60 s/frame
Temperature (°C)	25	25
Space group	$Cmc2_1$	$Cmc2_1$
a-axis length (Å)	5.6686(2)	5.6618(7)[a]
b-axis length (Å)	15.0060(9)	14.9981(12)[a]
c-axis length (Å)	7.6892(4)	7.6806(7)[a]
Cell volume ($Å^3$)	654.07(6)	652.21(12)[a]
Z	4	4
ρ (g/cm^3)	2.942	2.950
Reflections collected	4294	5915
Max. 2θ (deg)	69.93	69.94
Index range *h*	−9…9	−9…9
Index range *k*	−24…24	−24…23
Index range *l*	−12…12	−12…11
Resolution range (Å)	1…0.6	1…0.62
Unique reflections	1166	1130
Reflections $>2\sigma$(I)	1045	1088
R(int)	0.0510	0.0399
$R(\sigma)$	0.0375	0.0294
L.S. parameter no.	83	83
Goodness of fit	0.990	1.046
R_1; $I > 4\sigma Fo$	0.0173	0.0186
R_1; all data	0.0273	0.0199
wR_2 (on F^2)	0.0295	0.0370
$\Delta\rho_{min}$, close to	−0.21 e $Å^{-3}$, O1	−0.24 e $Å^{-3}$, Al1
$\Delta\rho_{max}$, close to	0.24 e $Å^{-3}$, B1	0.24 e $Å^{-3}$, Al2

[a] Lattice parameters measured with the CAD4.

probe. The ^{11}B and ^{27}Al MAS-NMR spectra were recorded at 128.38 and 104.26 MHz, respectively, using the following parameters: 0.3 µs $\pi/6$ pulse widths, 25 kHz MAS rate, 3 s (0.2 s for ^{27}Al) relaxation delays, appropriate number of scans for reasonable signal to noise ratios and 77 kHz SPINAL-64 proton decoupling [52]. ^{11}B and ^{27}Al chemical shifts were referenced to external samples of 1 M aqueous H_3BO_3 at 19.6 ppm [53] and 1.1 m $Al(NO_3)_3$ solution at 0.0 ppm [54]. The observed ^{27}Al NMR line shape was exactly the same when no proton decoupling was applied, whereas the ^{11}B quadrupolar powder pattern of, e.g. H_3BO_3 subtly depended on the efficiency of the decoupling field [55]. Owing to the presence of boron nitride devices in the probe, a ~16 kHz broad, asymmetric background signal was present in the ^{11}B NMR spectra. Before further analysis of these spectra, the background signal recorded with an empty spinner was subtracted from the spectrum of interest. Quadrupolar parameters and the relative amounts of $B^{(III)}$ and/or $B^{(IV)}$ atoms were determined by non-linear least-square fits of the regions of interest using the software Dmfit v. 20080716 [56]. For H_3BO_3, the parameters C_q=2.51 MHz, δ_{iso}=19.7 ppm and η=0.04 were in good accordance with literature data [55]. For resonances originating from single components only, the parameters for amplitude, position, quadrupolar coupling constant, asymmetry parameter and the zero order base line were automatically and independently optimized by the fit routine. In the case where $B^{(III)}$ and $B^{(IV)}$ resonances were observed simultaneously ($Al_4B_2O_9$ [39,40]), the asymmetry parameter was kept constant for the trigonal $B^{(III)}$ site and a Gaussian shape was chosen for tetrahedrally coordinated $B^{(IV)}$ in order to compare results to those of Fischer et al. [40]. ^{27}Al NMR parameters (δ_{iso}, C_q, η) were determined from slices of a z-filtered MQ-MAS-NMR spectrum and the 1D NMR spectra were subsequently simulated keeping the preliminary evaluated parameters C_q and η constant, while the parameters for amplitude, chemical shift and zero order base line were optimized.

3.4. FTIR and Raman spectroscopy

FTIR and Raman spectra were collected for sample *e* and Al_2BO_4 as reference for tetrahedrally coordinated BO_4. IR powder spectra were acquired from 300 to 4000 cm^{-1} on a Bruker Tensor 27 FTIR spectrometer equipped with a globar MIR light source, a KBr beam splitter, and a DLaTGS detector. Sample and background spectra

were averaged from 100 scans at 4 cm^{-1} resolution. Two methods were used to obtain absorption spectra: (1) the finely ground sample was dispersed in KBr (~1:200), pressed to transparent pellets, and measured in transmission mode in the usual sample compartment. (2) The undiluted sample powder was pressed on the diamond window of a Harrick MVP 2 diamond ATR accessory. Background spectra were obtained from a pure KBr pellet and from the empty ATR unit. Data handling was performed with OPUS v. 5.5 software [57].

Powder Raman spectra were obtained from 70 to 1670 cm^{-1} on a confocal edge filter-based Renishaw RM1000 micro-Raman system equipped with a 17 mW HeNe-laser (632.8 nm excitation) and a 50 mW multimode Ar^+-laser (488 and 514.5 nm excitation, each ~20 mW), a 1200 lines/mm grating, using a thermo-electrically cooled CCD detector. Raman intensities were collected with a Leica DMLM microscope with a 50 × /0.85 n.a. objective. Excitation at 488 nm and 10 min acquisition time yielded Raman spectra with reasonable signal to noise ratio at a resolution of 5–6 cm^{-1}. Data was processed with Grams32 software v. 4.14 [58].

3.5. Laser-ablation ICP-MS

Al_2O_3 and B_2O_3 wt% were measured in-situ on epoxy-embedded single-crystals from samples *a* and *f* (Table 3) by laser-ablation inductively coupled plasma mass-spectrometry (LA ICP-MS). The system consists of a pulsed 193 nm ArF Excimer laser Geolas Pro system (Lambda Physik, Germany) coupled with a Perkin Elmer ELAN DRCe quadrupole mass spectrometer. Details on the setup and optimization strategies to minimize matrix effects by setting up robust plasma conditions can be found in Pettke [59].

Al_2O_3 inclusion-free crystal domains in sample *a* were usually smaller than 50 μm; hence, the beam diameter for analysis was set to 32 μm. To minimize matrix-load induced elemental fractionation [60], ablation rate tests were performed at 6 J/cm^2 energy density on the sample with a 10 Hz pulse rate, revealing a much higher ablation rate for NIST SRM 610 used for calibration than for the aluminoborate crystals. Calibration shots were thus made with 16 μm beam size, resulting in near-equal aerosol masses ablated per unit time. Only 10 s signals were used for quantification, to ensure a crater aspect (depth/diameter) ratio < 1. The aerosol was transported to the ICP-MS using mixed He–Ar gas. For samples *a* and *f*, a total of 11 and 12 individual spot analyses were acquired, respectively. Data quantification was done using SILLS v. 1.2.0 [61], employing 356 ± 7 μg/g for B [62] and 2.04 wt% Al_2O_3. Internal standardization was carried out by summing B_2O_3 and Al_2O_3 to 100 wt%.

4. Results

4.1. X-ray diffraction

Single-crystal X-ray (CAD4) refined cell dimensions of sample *a* yielded $V=654.07(6)$ Å^3 whereas corresponding parameters (CAD4) for sample *f* were significantly smaller: $V=652.21(12)$ Å^3 (Table 4).

Three refinement strategies were followed for both crystals *a* and *f*: (1) the structures were refined with all positions fully occupied. (2) The occupancy of the Al4 tetrahedron was fixed at 9% B → Al substitution according to the suggestion of Ihara et al. [42], and (3) a mixed Al, B population was refined at each Al site in separate refinements. In strategy (3), intensity data were restricted to $0.6 \le \lambda/(2\sin\theta) \le 1$ Å (high angle data) in order to reduce contributions from bonding electrons. X-ray diffraction data containing bonding electron information are not properly modeled in standard site-occupancy refinements and lead to incorrect occupancy fractions [63].

After refinement in accordance with model (1), atomic displacement parameters ($U_{eq.}$) were very similar for all Al sites except for Al2. $U_{eq.}$ of Al2 was about 12% higher than the average of the remaining three.

Strategy (2) led to increased least squares agreement factors compared to (1) and most important, the atomic displacement parameter of the tetrahedrally coordinated Al4 site decreased to ca. 50% of the value refined in strategy (1).

Strategy (3) resulted in fully occupied Al polyhedra, except for Al2. This type of population refinement has to be performed stepwise for each Al site to reduce correlations with the scale factor. Due to correlations between displacement parameters and occupancy, vacancies at the Al2 site were also refined with an isotropic displacement parameter of Al2 constrained to the one of Al3. No significant difference in vacancy concentration was observed, thus, we chose to refine all displacement parameters individually. For Al2, final occupancies were Al:B=0.973(5):0.027(5) for sample *a* and Al:B=0.962(6):0.038(6) for sample *f*. As an alternative approach, Al vacancies were refined at the Al2 site, resulting in 2.1(4)% vacancies for sample *a* and 3.2(4)% for sample *f*. All refinements of strategy (3) reduced the originally (according to strategy 1) enlarged atomic displacement factor $U_{eq.}$ of Al2 to values similar to the ones of other Al sites within the same structure.

Atomic coordinates, isotropic and anisotropic displacement parameters of the vacancy model (strategy 3) for samples *a* and *f* and calculated bond valences of sample *a* are listed in Appendix A.

The main features of the structure (Fig. 3) are isolated mullite-like chains of edge-sharing Al1 octahedra running parallel to the *a*-axis. Compared to mullite, the cell is doubled along [100] and [010] resulting in an additional symmetry equivalent octahedral chain at *b*/2. Proximate octahedral chains are connected by pairs of irregular edge-sharing AlO_5 polyhedra (Al2 and Al3) and, additionally, by alternating AlO_4 tetrahedra (Al4) and BO_3 triangles (B1). One side of an edge-connected AlO_5 polyhedra pair is edge-connected to octahedra and corner-linked to BO_3 triangles, whereas the other side is edge-connected to octahedra and corner-linked to tetrahedra. As a result, octahedral chains are separated along [010] by two different alternating segments within (101). One segment comprises AlO_4 and AlO_5 polyhedra (segment 1, Fig. 3); the other consists of BO_3 and AlO_5 polyhedra (segment 2). The Al1 octahedron, the tetrahedron and the BO_3 triangle are rather regular: $\Delta(Al1–O)_{max}=0.0553$ Å, $\Delta(Al4–O)_{max}=0.0250$ Å and $\Delta(B1–O)_{max}=0.0138$ Å, whereas the AlO_5 polyhedra are fairly distorted with $\Delta(Al2–O)_{max}=0.2966$ Å, and $\Delta(Al3–O)_{max}=0.3692$ Å (Appendix A). The AlO_5 polyhedra are more precisely described as AlO_{4+1} as Al occupies the center of the four closest O ligands, which is also responsible for the increased distortion.

After preferred-orientation corrections in powder Rietveld refinements, all patterns from samples *a–f* were matching the Al_5BO_9 structure, differing only in the amount of excess corundum. Pawley-refinement-derived lattice parameters of all samples are shown in Table 5. They are the same within a maximum deviation of six esd's, except for the significantly smaller values of sample *f*, confirming our previous single-crystal results. Excess corundum was only found in samples *a–c* (Table 3) whereas no corundum was found in samples *d–f*, prepared with excess B_2O_3/H_3BO_3 in the starting mixtures (Table 5).

4.2. Solid-state ^{11}B and ^{27}Al MAS-NMR

In the ^{11}B MAS-NMR spectrum of $Al_4B_2O_9$, which was collected as a reference, signals of highly symmetric four-fold coordinated

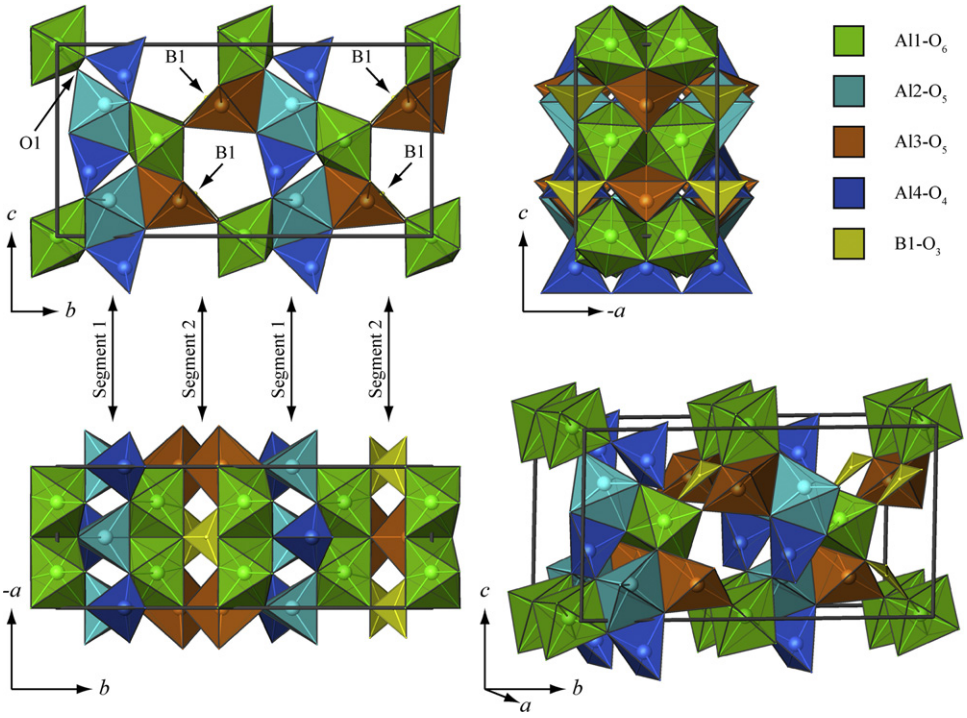

Fig. 3. Structural drawing of an Al_5BO_9 unit cell projected along the *a*-axis (top left), the *b*-axis (top right), the *c*-axis (bottom left) and in an arbitrary view (bottom right). Segments dividing the mullite-like AlO_6 chains are indicated with arrows: Segment 1 consists of Al2–O_5 polyhedra and Al4–O_4 tetrahedra, whereas segment 2 contains Al3–O_5 polyhedra and B1–O_3 triangles. Note that Al2 and Al3 atoms are not in the center of the polyhedron. For better illustration of the similarity to the mullite structure, the unit cell has been shifted by 0; 0.1164; 0.5.

Table 5
Lattice parameters and excess Al_2O_3 content of all samples determined by powder X-ray diffraction. For better comparison, lattice parameters obtained from single-crystal XRD are given in the bottom two rows.

Sample	*a* (Å)	*b* (Å)	*c* (Å)	*V* (Å^3)	GoF	Al_2O_3 (wt%)
a	5.66848(4)	15.00512(12)	7.68971(5)	654.057(8)	1.04	8
b	5.66738(3)	15.00687(10)	7.69230(4)	654.225(7)	1.52	7
c	5.66789(4)	15.00604(14)	7.69157(6)	654.188(9)	1.47	8
d	5.66775(3)	15.00642(6)	7.68943(3)	654.006(5)	1.60	0
e	5.66869(2)	15.00741(7)	7.69005(3)	654.211(5)	1.47	0
f	5.66421(3)	15.00214(7)	7.68428(3)	652.974(5)	1.83	0
a [a]	5.6686(2)	15.0060(9)	7.6892(4)	654.07(6)	n/a	n/a
f [a]	5.6618(7)	14.9981(12)	7.6806(7)	652.21(12)	n/a	n/a

[a] Lattice parameters from single-crystal XRD for comparison.

$B^{(IV)}$ and second-order quadrupolar broadened planar three-fold coordinated $B^{(III)}$ were observed at distinct positions (Fig. 4). The ratio of ~25:75 determined by line shape analysis for the $B^{(IV)}/B^{(III)}$ sites fits reasonably to the value of ~20:80 estimated by Fischer et al. [40]. Nevertheless, accurate quantitative results can only be evaluated including the signal intensities of spinning sidebands.

The ^{11}B MAS-NMR spectra of samples *a*–*f* showed the same shapes of resonances (Fig. 4). Chemical shifts and quadrupolar parameters obtained by line shape analysis (Table 6) yielded convergent results for all synthesis routes (Table 3). The influence of a simulated $B^{(IV)}$ signal on the expected experimental line shape of sample *a* is shown in Fig. 5. For fractions as low as 2–3% of $B^{(IV)}$, a distinct deviation of the quadrupolar broadened line shape of the spectra can be observed. As shown in Fig. 4, none of the measured ^{11}B MAS-NMR spectra suggest evidence for $B^{(IV)}$.

^{27}Al MAS-NMR spectra of samples *a*–*f* match each other (Fig. 6), only the amount of excess corundum varies, depending on synthesis conditions. In the ^{27}Al 3Q-MAS-NMR spectrum of sample *a* (Appendix A) at least three distinct aluminum species were observed and from chemical shift arguments $Al^{(IV)}$, $Al^{(V)}$ and $Al^{(VI)}$ are present. The spectrum showed the same resonances already observed by Gan et al. [44], recorded at the same magnetic field. Since they also collected MQ-MAS data at higher frequencies, it is evident that two different $Al^{(V)}$ sites are present. DOR NMR diffusion experiments [45] allowed assignment of the $Al^{(V)}$ signals to $Al_1^{(V)}$ (Al2 in this study) and $Al_2^{(V)}$ (Al3 in this study). All 1D ^{27}Al MAS-NMR line shape simulations performed in our study (Fig. 7) yielded four different Al species: $Al^{(IV)}$, $Al_1^{(V)}$, $Al_2^{(V)}$ and $Al^{(VI)}$ (Appendix A) with a ratio of ca. 1:1:1:2. The shape of the 1D ^{27}Al NMR spectra of samples *d* and *e* (lowest amounts of Al_2O_3) are both in perfect agreement with literature data [43].

4.3. Raman and FTIR spectroscopy

FTIR powder spectra are shown in Fig. 8. Note that IR band positions from the KBr and ATR techniques are almost identical, although different intensities result in somewhat different band patterns. Moreover, compared to KBr spectra, ATR band positions are systematically shifted to slightly lower values, which is a common

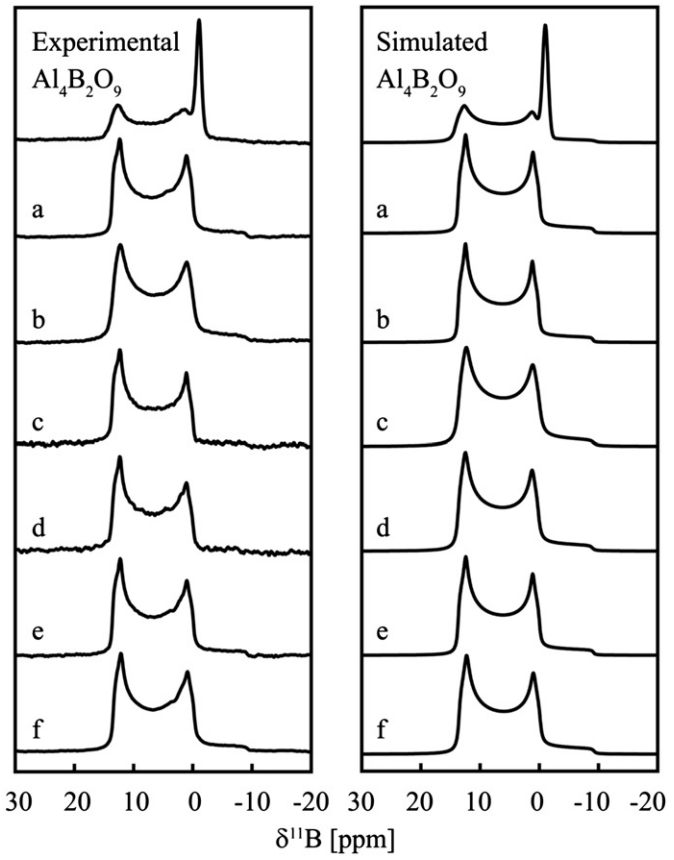

Fig. 4. Experimental and simulated $^{11}B\{^1H\}$ MAS-NMR spectra (128.38 MHz) of reference $Al_4B_2O_9$ powder (top) and powdered samples *a–f*. In the spectra of $Al_4B_2O_9$, the narrow resonance around −1 ppm is assigned to BO_4.

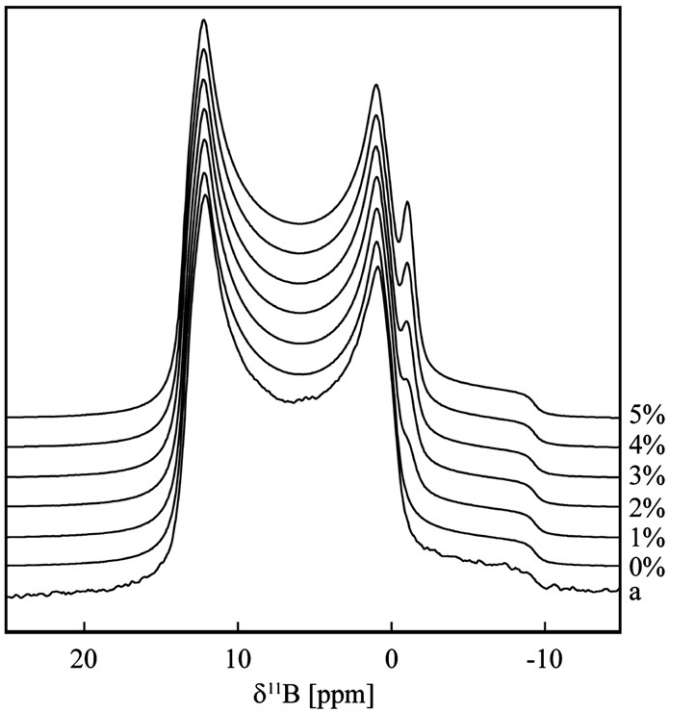

Fig. 5. Experimental $^{11}B\{^1H\}$ MAS-NMR spectra of powdered single-crystals from sample *a* with a series of simulated spectra considering the signals of 0–5% tetrahedrally coordinated BO_4.

Table 6
Chemical shifts and ^{11}B quadrupolar parameters obtained by line shape simulation.

Sample	$\delta^{11}B_{iso}$ (ppm)	C_q (MHz)	η
H_3BO_3	19.7	2.51	0.04
$Al_4B_2O_9$[a]	17.4	2.66	0.10
a	16.8	2.62	0.09
b	16.7	2.61	0.09
c	16.8	2.61	0.09
d	16.8	2.61	0.08
e	16.8	2.62	0.08
f	16.7	2.61	0.09

[a] The four-fold coordinated ^{11}B site was simulated by a Gaussian shape at −1.0 ppm (line width of ~140 Hz). Ratio determined: $B^{(III)}/B^{(IV)}$~75:25.

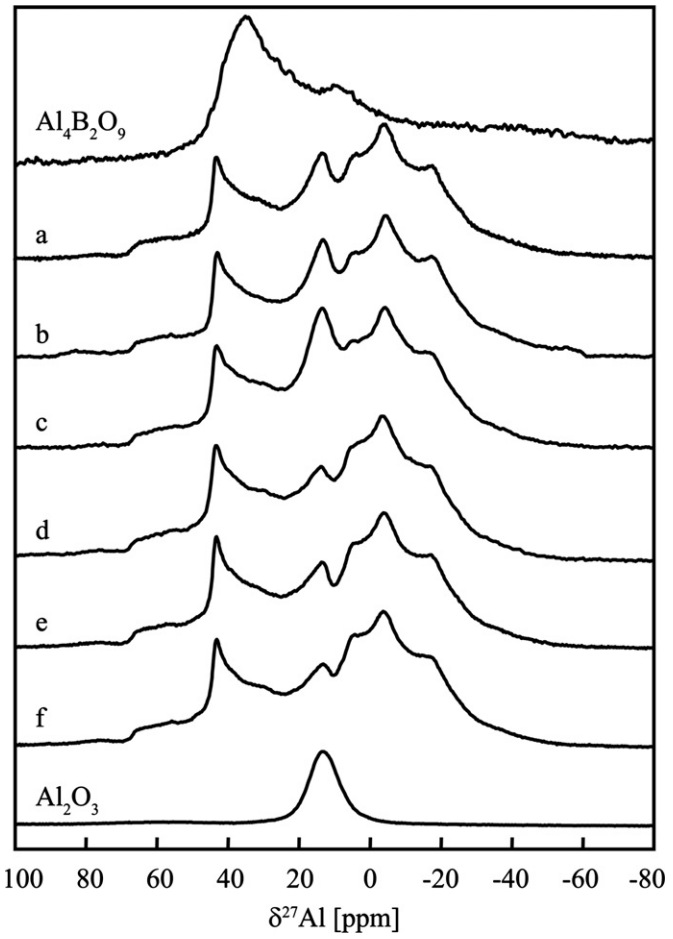

Fig. 6. 1D ^{27}Al MAS-NMR spectra (104.26 MHz) of $Al_4B_2O_9$ (top), samples *a–f* and pure corundum (bottom).

effect in ATR spectra [64]. In contrast, due to different selection rules, Raman spectra appear quite different (Fig. 9). Considering the structural units of the investigated borates, the spectral regions (both IR and Raman) may be assigned to certain vibrations. The antisymmetric stretching vibrations of the BO_3 group are expected at ~1450–1200 cm^{-1} (predominant in IR spectra, Fig. 8), the symmetric stretching vibration at ~900–1050 cm^{-1} (predominant in Raman spectra, Fig. 9). The characteristic IR-active antisymmetric stretching bands of the BO_4 tetrahedron in the vibrational region at ~950–1200 cm^{-1} are only observed for the $Al_4B_2O_9$ reference but not in sample *e* (Fig. 8). The strong BO_3 characteristic symmetric stretching mode of the BO_3 group occurs in Raman spectra at 1016 cm^{-1} (Fig. 9). The Raman spectrum of the reference material $Al_4B_2O_9$ shows in addition a strong BO_4 characteristic band at ~960 cm^{-1}, which is absent in sample *e* (Fig. 9). The bending motions of the BO_3 group and

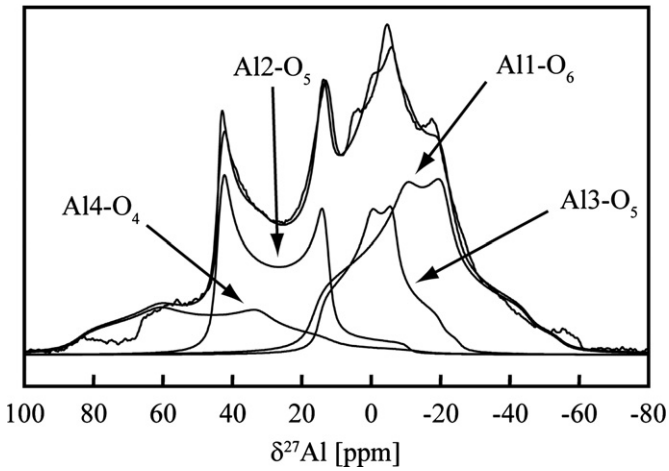

Fig. 7. 1D ^{27}Al MAS-NMR spectrum of sample *b* with spectrum simulation using the quadrupolar parameters extracted from simulation of the ^{27}Al 3Q-MAS-NMR spectrum.

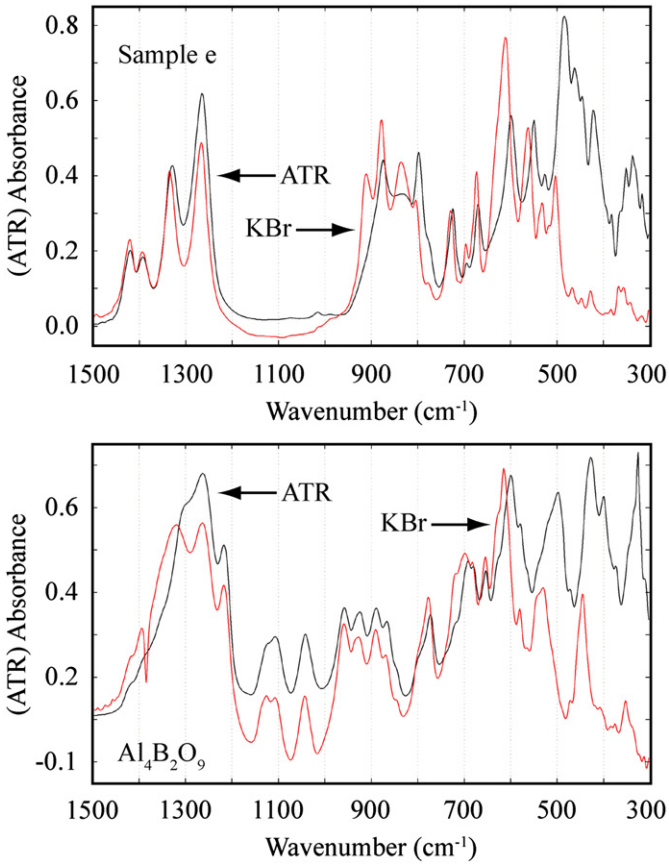

Fig. 8. ATR and KBr pellet FTIR spectra of sample *e* (top) and $Al_4B_2O_9$ (bottom). The well resolved peaks between 1250 and 1450 cm^{-1} (top) are assigned to the BO_3 group in sample *e*. Peaks of stretching vibrations of BO_4 in reference $Al_4B_2O_9$ (bottom) are between 950 and 1200 cm^{-1} (bottom). In the spectra of sample *e*, no indication for BO_4 can be found.

all other vibrations of the AlO_x polyhedra and lattice vibrations are contained in the complex band region between 900 and 100 cm^{-1}. Because of this complexity, the latter will not be discussed.

To answer the question for boron speciation ($B^{(III)}$ and/or $B^{(IV)}$ coordination, one or more structural sites) the possible vibrations of a BO_3 group need to be considered. The ideal anion group (e.g. in solution or in a calcite-type structure) has symmetry D_{3h} resulting

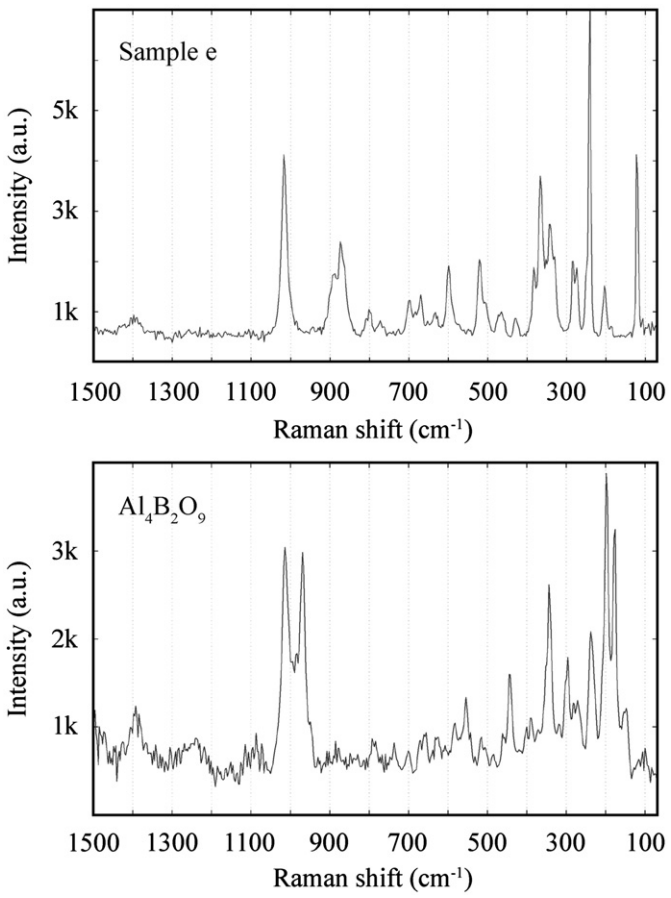

Fig. 9. Raman spectra of sample *e* (top) and reference $Al_4B_2O_9$ (bottom). The single strong Raman band at 1016 cm^{-1} is assigned to the symmetric stretching mode of the BO_3 group (top), whereas the double peak in the $Al_4B_2O_9$ pattern corresponds to vibrations of BO_3 and BO_4 groups.

in four possible vibrations (Appendix A). Two of them, i.e. the E' species v_3 and v_4, are doubly degenerate and active in both IR and Raman spectra. In contrast, v_1 is only Raman-active and v_2 is only IR-active. If the symmetry of the BO_3 group is lowered in a crystal structure, the degenerate E' species split into two bands, and formerly inactive vibrations may become active. In Al_5BO_9 the Wyckoff site of boron is 4*a* with site symmetry *m* (Appendix A). The effective symmetry of the BO_3 group, however, is higher, as is indicated by the very similar bond lengths of B–O3 (1.36 Å) and $2 \times$ B–O7 (1.38 Å) (Appendix A), and almost identical bond angles close to 120°, i.e. it represents a flat isosceles triangle with symmetry C_{2v} (*mm*2). Independently, if the true site symmetry or the effective symmetry are preferred, the vibrational E' modes split up and the selection rules are released.

In addition to the symmetry considerations above, it is important to note that boron consists of two abundant natural isotopes ^{11}B and ^{10}B with a ratio of about 80:20 [65]. This isotope ratio is also found in the common boron-bearing chemicals, such as B_2O_3 and H_3BO_3 used in the syntheses of the present study. Due to the different mass of the isotopes (10 rel%), the frequencies of vibrations, where motions of boron isotopes are involved (therefore not in v_1!), are different by several tens of cm^{-1} [66–68].

4.4. Laser-ablation ICP-MS

LA ICP-MS measurement data for samples *a* and *f* are reported in Table 7. Compositions of the two synthetic products are identical. They are marginally higher with ~12.35 wt% B_2O_3 than expected

for pure Al_5BO_9 (12.01 wt% B_2O_3), but significantly lower than for $Al_{18}B_4O_{33}$ (13.17 wt% B_2O_3, Table 1). External reproducibility of one standard deviation uncertainties on B_2O_3 are ca. 0.25 wt%, which is of the same order as the uncertainty quoted for the B concentration of the standard reference material NIST SRM 610 used for calibration [62].

5. Discussion

The excellent agreement of cell dimensions (Table 5) of samples *a*–*e* synthesized along different routes and starting compositions suggests that they are structurally and chemically very similar differing in the amount of excess corundum. This is also confirmed by ^{11}B and ^{27}Al MAS-NMR data (Figs. 4 and 6, Table 6). LA ICP-MS compositional data of samples *a* and *f* are equal within esd's (Table 7). Atomic coordinates of samples *a* and *f* (single-crystal X-ray data) are also identical. Indications for differences between samples *a* and *f* are: (1) the cell dimensions (Table 5), which are most sensitive due to their ability to sum up small structural differences, (2) the crystal from sample *f* had also systematically larger atomic displacement parameters than the crystal from sample *a* (ca. 20% for cation sites, corresponding to ca. 10 esd's, and ca. 10% for O sites, corresponding to 5 esd's). Both data sets were of corresponding quality but were measured on different machines. Nevertheless, we have previously tested reference crystals to corroborate that both machines produce comparable results. Thus, the increased displacement parameters of sample *f* must be related to crystal properties, such as increased strain compared to the crystal from sample *a*. The only systematic experimental difference between samples *a*–*e* and sample *f*, distinct by their unit cell volumes (Table 5), is the higher synthesis temperature for sample *f* (at 1550 °C cooled to 1250 °C) whereas samples *a*–*e* were treated at 1200 °C or below. The higher crystallization temperature and subsequent air quenching to ambient conditions could explain the suspected increased strain. But is B→Al substitution the origin of the significantly smaller unit cell volume of sample *f*? LA ICP-MS results (Table 7) seem to exclude this interpretation. A possible answer will be discussed below.

The 'hypothetical' $Al_{18}B_4O_{33}$ ($=Al_{4.91}B_{1.09}O_9$) composition with the structure of Al_5BO_9 can only be achieved if:

(1) 9% B substitutes for Al at the Al4 tetrahedron according to Ihara et al. [42]. B is only known in three- and four-fold coordination by O [31,69]. Therefore, B is not expected to occupy one of the other five- or six-fold coordinated sites within the mullite type Al_5BO_9 structure.
(2) Minor Al vacancies at one of the other Al sites (six-coordinate Al1 or five-coordinate Al2 and Al3) may be charge balanced by a BO_4 or BO_3 polyhedron at a nearby interstitial position. In case of $Al_{18}B_4O_{33}=Al_{4.91}B_{1.09}O_9$, 9% Al vacancies may either be located (2*a*) at one single position, or (2*b*) 9% vacancies are statistically distributed throughout all Al positions in the structure.

Table 7
Al_2O_3 and B_2O_3 concentrations (wt%) from LA ICP-MS.

Spot no.	Sample *a*		Sample *f*	
	Al_2O_3	B_2O_3	Al_2O_3	B_2O_3
1	87.71	12.29	87.65	12.35
2	87.75	12.25	87.65	12.35
3	87.63	12.37	87.99	12.01
4	87.72	12.28	87.33	12.67
5	87.69	12.31	87.72	12.28
6	87.75	12.25	87.29	12.71
7	87.60	12.40	87.72	12.28
8	87.72	12.28	87.69	12.31
9	87.84	12.16	87.78	12.22
10	87.09	12.91	87.08	12.92
11	87.71	12.29	87.89	12.11
12	87.86	12.14	n/a	n/a
Average	87.66	12.33	87.62	12.38
ESD	0.20	0.20	0.27	0.27
ESD SRM 610[a]	n/a	0.25	n/a	0.25

[a] Standard deviation according to uncertainty of NIST SRM 610 [62].

Ad (1): Single-crystal XRD investigations on crystals from samples *a* and *f* do not show any indication for the 9% B→Al4 substitution as proposed by Ihara et al. [42]. If applying a constraint of 9% B and 91% Al to the tetrahedral Al4 site, agreement factors increase (*R*1: from 0.0198 to 0.0203 for sample *a* and 0.0212 to 0.0218 for sample *f*) and most important, the atomic displacement factor ($U_{eq.}$) at Al4 becomes halved. This $U_{eq.}$ behavior has a straightforward explanation: if the electron density (occupancy) at a structural site is underestimated in the refinement model, the probability density cloud around the atomic site (represented by $U_{eq.}$) contracts because integration over the observed electron density is already satisfied (according to the model) for a smaller cloud volume. Theoretically [30] the opposite should be observed: occupational disorder leads to increased displacement parameters. Furthermore, the Al4 tetrahedron is rather undistorted with $\Delta(Al4–O)_{max}=0.0250$ Å and the average bond length $<Al4–O>_{tet}=1.7464(12)$ Å is in agreement with a fully occupied AlO_4 tetrahedron [30]. By assuming a mean tetrahedral bond length for BO_4 of 1.476 Å [31], the average bond length of a tetrahedron occupied with 91% Al and 9% B is expected to be ~1.72 Å.

^{11}B MAS-NMR spectra show no evidence for tetrahedrally coordinated $B^{(IV)}$ in samples *a*–*f*. Due to the low detection limit and the good agreement of the $B^{(IV)}$:$B^{(III)}$ ratio for $Al_4B_2O_9$ [40], partially occupied tetrahedral BO_4 sites with occupancies >2% should be clearly detectable (Fig. 5). From FTIR spectra, 9% of $B^{(IV)}$ in tetrahedral coordination can also be excluded, because the characteristic vibrational region of the IR-active antisymmetric stretching vibrations of the BO_4 tetrahedron at ~950–1200 cm^{-1} [67] is empty (Fig. 8). Moreover, there is only one Raman band at 1016 cm^{-1} (Fig. 9) that can unequivocally be assigned to the symmetric stretching mode of the BO_3 group; hence, no band is left to be assigned to ν_1 of a potential BO_4 group.

Ad (2a): Site occupancy refinements on crystals *a* and *f* provided no evidence for 9% vacancies at Al1, Al2 or Al3. In addition, all spectroscopic methods applied in this study yielded no indication of additional BO_4 or BO_3 with 9% occupancy.

The single, strong Raman band at 1016 cm^{-1} (Fig. 9) does not suggest an additional BO_3 group occupied to 9%. Within detection limits (2–3%), IR and Raman spectra (Figs. 8 and 9 and Appendix A) are consistent with assumption of a single BO_3 group, considering both natural B isotopes. The symmetric stretching mode ν_1 is visible only as a very weak band at 1015 cm^{-1} in IR spectra (IR active due to distortion from the ideal symmetry of the planar BO_3 group). The different B isotopes do not split this mode, as the central B atom is almost inert during this vibration. A similar position (1017/1019 cm^{-1}) of this ν_1 mode was observed in Raman spectra of another aluminoborate with additional REEs by Xia et al. [70]. The antisymmetric stretching mode (doubly degenerate in case of ideal planar symmetry) is split into two modes by the lower site symmetry and further doubled by the two B isotopes. The resulting four bands are clearly visible between 1250 and 1450 cm^{-1} in the IR spectra, whereas only two very weak bands are observed around 1400 cm^{-1} in Raman spectra [70].

Ad (2b): The hypothesis that ca. 9% vacancies are distributed over several Al polyhedra ($Al1^{(VI)}$, $Al2^{(V)}$, $Al3^{(V)}$, and $Al4^{(IV)}$) and for charge balance BO_3 triangles at nearby interstitial positions are

occupied, can also be rejected based on the above spectroscopic arguments. Most convincing, results of LA ICP-MS measurements clearly show that the investigated crystals of samples *a* and *f* cannot have a composition of $Al_{18}B_4O_{33}$. Averaged LA ICP-MS data of 12.36 wt% B_2O_3 with a standard deviation of 0.25 wt% result in $Al_{4.99}B_{1.01}O_9 \leq Al_{4.97}B_{1.03}O_9 \leq Al_{4.95}B_{1.05}O_9$. Due to reasons mentioned above (e.g., similarity in unit cell volumes), it is very likely that these values apply for all samples.

One of the striking results of structure refinements presented in this study is the significantly large $U_{eq.}$ value for Al2 compared to all other Al sites. This observation is consistent with previous, less accurate structural data [4,25,42]. Results of single-crystal structure refinements allow the interpretation of a small amount B at Al2 (2.7(5)% for sample *a* and 3.8(6)% for sample *f*). In corresponding refinements, displacement parameters for the Al2 site are no longer larger than those of the other Al sites in refinements with fully occupied cation sites (Appendix A). In this model B occupies the center of the tetrahedron formed by O1, $2 \times$ O2 and O5. From $^{11}B\{^1H\}$ MAS-NMR simulations BO_4 with more than ca. 2% occupancy in addition to BO_3 can be excluded for samples *a* and *f* (Fig. 5). On the other hand, the average of the four shortest Al2–O distances is ca. 1.79 Å. It seems that this type of substitution is rather unlikely, considering the large size difference due to the characteristic tetrahedral B–O bond length of 1.476 Å.

An X-ray site occupation refinement is mainly sensitive on the number of scattering electrons. Thus alternatively to partial B occupancy, 2.1(4)% and 3.2(4)% vacancies at Al2 may also be successfully modeled for samples *a* and *f*, respectively. In this case, we assume interstitial B in three-fold coordination for charge balance. The Al2 polyhedron comprises 5 oxygen ligands, of which O1 has the lowest bond valence (Appendix A). Therefore, a new boron position must be close to the Al2 site and close to O1. Due to the low occupancy, no distinct new boron position could be found in difference Fourier-maps of single-crystal X-ray structure refinements (2% B is equal to an electron density of 0.10e). Nevertheless, we assume that the new boron position is centered within one of the three faces of the Al2 polyhedron sharing O1 as apex. A similar substitution is known from the natural mullite-type borosilicate werdingite [71], in which BO_3 groups are correspondingly disordered with Al tetrahedra. If the interstitial boron site in Al_5BO_9 is statistically distributed among all three faces, it is below the detection limit of FTIR/Raman or single-crystal X-ray diffraction methods. Low concentrations of vacancies at Al2 with B in three-fold coordination distributed in the O1–O5–O2 (twice due to symmetry equivalent sites) and the O1–O2–O2 faces would locally distort the structure because O–O separations are much shorter in BO_3 than in the irregular AlO_5 polyhedron. Therefore, slightly different concentrations of vacancies at the Al2 position compensated by interstitial BO_3 polyhedra could explain the observed difference in cell parameters of samples *a* and *f*.

None of the Al_2O_3-rich mullite-type aluminoborates synthesized above 1100 °C had $Al_{18}B_4O_{33}$ composition. The exact stoichiometry is close to Al_5BO_9. Values derived from single-crystal diffraction data suggest $Al_{5-x}B_{1+x}O_9$ with $0.021(6) < x < 0.038(6)$, which agrees with compositional data from LA ICP-MS yielding $x = 0.03(2)$. Considering the historical background, it is assumed that the claimed $Al_{18}B_4O_{33}$ stoichiometry is probably an artifact due to old inaccurate chemical analyses.

Acknowledgments

This study was financed by the Swiss National Science Foundation, Grant 200020-112198 'Crystal Chemistry of Minerals'. We thank Ruth Maeder for lab assistance, Mariko Nagashima for the translation of Japanese articles and Evgeny Galuskin and Piotr Dzierzanowski for providing EPMA data and images and Eva Wadoski for English corrections.

Appendix A. Supporting information

Supplementary data associated with this article can be found in the online version at doi:10.1016/j.jssc.2010.10.032.

Appendix B. Structural information

Crystal structure data according to the vacancy model refinement (strategy 3) of sample *a* can be obtained from Fachinformationszentrum Karlsruhe FIZ, 76344 Eggenstein-Leopoldshafen, Germany (fax: +49 7247 80 86 66; crysdata@fiz.karlsruhe.de) under depository number: CSD-422062.

References

[1] H. Schneider, S. Komarneni, Mullite, Wiley-VCH, Weinheim, 2005.
[2] G. Werding, W. Schreyer, Geochim. Cosmochim. Acta 48 (6) (1984) 1331–1344.
[3] G. Werding, W. Schreyer, Reviews in Mineralogy, vol. 33: Boron, in: E.S. Grew, L.M. Anovitz (Eds.), Mineralogical Society of America, Washington, DC, 1996, pp. 117–163.
[4] E.V. Sokolova, A.V. Azizov, M.A. Simonov, N.I. Leoniuk, N.V. Belov, Dokl. Akad. Nauk SSSR 243 (3) (1978) 655–658.
[5] J.J. Capponi, J. Chenavas, J.C. Joubert, Bull. Soc. Fr. Mineral. Cristallogr. 95 (3) (1972) 412–417.
[6] A. Vegas, F.H. Cano, S. Garciablanco, Acta Crystallogr. B. 33 (1977) 3607–3609.
[7] R.X. Fischer, H. Schneider, Eur. J. Mineral. 5 (20) (2008) 917–933.
[8] I.S. Buick, E.S. Grew, T. Armbruster, O. Medenbach, M.G. Yates, G.E. Bebout, G.L. Clarke, Eur. J. Mineral. 20 (5) (2008) 935–950.
[9] J.G. White, A. Miller, R.E. Nielsen, Acta Crystallogr. 19 (1965) 1060–1061.
[10] J. Jing, Y. Tao, G.B. Li, F.H. Liao, Y.X. Wang, L.P. You, J.H. Lin, Chem.-Eur. J. 10 (16) (2004) 3901–3906.
[11] S.W. Kim, S.G. Lee, J.K. Kim, J.Y. Kwon, H.C. Park, S.S. Park, J. Mater. Sci. 39 (4) (2004) 1445–1447.
[12 H.S. Song, J. Zhang, J. Lin, S.J. Liu, J.J. Luo, Y. Huang, E.M. Elssfah, A. Elsanousi, X.X. Ding, J.M. Gao, C.C. Tang, J. Phys. Chem. C 111 (3) (2007) 1136–1139.
[13] J. Zhang, J. Lin, H.S. Song, E.M. Elssfah, S.J. Liu, J.J. Luo, X.X. Ding, C. Tang, S.R. Qi, Mater. Lett. 60 (27) (2006) 3292–3295.
[14] J. Wang, G.L. Ning, X.F. Yang, Z.H. Gan, H.Y. Liu, Y. Lin, Mater. Lett. 62 (8–9) (2008) 1208–1211.
[15] H. Wada, K. Sakane, T. Kitamura, H. Hata, H. Kambara, J. Mater. Sci. Lett. 10 (18) (1991) 1076–1077.
[16] V.A. Sokolov, M.A. Gasparyan, Refract. Ind. Ceram. 45 (3) (2004) 177–180.
[17] L.M. Peng, X.K. Li, H. Li, J.H. Wang, M. Gong, Ceram. Int. 32 (4) (2006) 365–368.
[18] S.R. Qi, J. Zhang, J. Lin, H.S. Song, E.M. Elssfah, S.J. Liu, J.J. Luo, X.X. Ding, C. Tang, Mater. Lett. 60 (27) (2006) 3292–3295.
[19] E.M. Elssfah, H.S. Song, C.C. Tang, J. Zhang, X.X. Ding, S.R. Qi, Mater. Chem. Phys. 101 (2–3) (2007) 499–504.
[20] S.P. Ray, J. Am. Ceram. Soc. 75 (9) (1992) 2605–2609.
[21] T. Xinyong, W. Xinnan, L. Xiaodong, Nano Lett. (2007) 3172–3176.
[22] G.D. Gatta, N. Rotiroti, M. Fisch, T. Armbruster, Phys. Chem. Miner. 37 (4) (2010) 227–236.
[23] H. Wada, K. Sakane, T. Kitamura, M. Sunai, N. Sasaki, J. Mater. Sci. Lett. 12 (22) (1993) 1735–1737.
[24] H. Wada, K. Sakane, T. Kitamura, Y. Kayahara, A. Kawahara, N. Sasaki, J. Ceram. Soc. Jpn. 102 (8) (1994) 695–701.
[25] M. Garsche, E. Tillmanns, H. Almen, H. Schneider, V. Kupcik, Eur. J. Mineral. 3 (5) (1991) 793–808.
[26] R.Z. Ma, Y. Bando, T. Sato, C.C. Tang, F.F. Xu, J. Am. Chem. Soc. 124 (36) (2002) 10668–10669.
[27] Y. Li, R.P.H. Chang, Mater. Chem. Phys. 97 (1) (2006) 23–30.
[28] J. Zhang, Y. Huang, J. Lin, X.X. Ding, Z.X. Huang, S.R. Qi, C.C. Tang, J. Phys. Chem. B 109 (27) (2005) 13060–13062.
[29] W.D. Fei, H.Y. Yue, L.D. Wang, Mater. Chem. Phys. 119 (3) (2010) 515–518.
[30] M. Kunz, T. Armbruster, Am. Mineral. 75 (1-2) (1990) 141–149.
[31] F.C. Hawthorne, P.C. Burns, J.D. Grice, Reviews in Mineralogy, vol. 33: Boron, in: E.S. Grew, L.M. Anovitz (Eds.), Mineralogical Society of America, Washington, DC, 1996, pp. 41–115.
[32] E. Mallard, C. R. 105 (1887) 1260–1265.
[33] J.J. Ebelmen, C. R. 32 (1851) 330–333.
[34] M. Websky, Sitzungsber. Königlich Preuss. Akad. Wissen. Berlin (2) (1883) 671–675.
[35] R.C. Benner, H.N. Baumann, United States Patent Office, 2.118.143, 1938.
[36] H.N. Baumann, C.H. Moore, J. Am. Ceram. Soc. 25 (14) (1942) 391–394.
[37] A. Dietzel, H. Scholze, Glastech. Ber. 28 (2) (1955) 47–52.
[38] H. Scholze, Z. Anorg. Allg. Chem. 284 (4–6) (1956) 272–277.
[39] D. Mazza, M. Vallino, G. Busca, J. Am. Ceram. Soc. 75 (7) (1992) 1929–1934.

[40] R.X. Fischer, V. Kahlenberg, D. Voll, K.J.D. MacKenzie, M.E. Smith, B. Schnetger, H.J. Brumsack, H. Schneider, Am. Mineral. 93 (5–6) (2008) 918–927.
[41] P.J.M. Gielisse, W.R. Forster, Nature 195 (1962) 69–70.
[42] M. Ihara, K. Imai, J. Fukunaga, N. Yoshida, Yogyo Kyokai Shi 88 (1014) (1980) 77–84.
[43] D. Massiot, D. Muller, T. Hubert, M. Schneider, A.P.M. Kentgens, B. Cote, J.P. Coutures, W. Gessner, Solid State Nucl. Magn. Reson. 5 (2) (1995) 175–180.
[44] Z.H. Gan, P. Gor'kov, T.A. Cross, A. Samoson, D. Massiot, J. Am. Chem. Soc. 124 (20) (2002) 5634–5635.
[45] I. Hung, A.P. Howes, T. Anupold, A. Samoson, D. Massiot, M.E. Smith, S.P. Brown, R. Dupree, Chem. Phys. Lett. 432 (1–3) (2006) 152–156.
[46] K.J.D. MacKenzie, M.E. Smith, T.F. Kemp, D. Voll, Appl. Magn. Reson. 32 (4) (2007) 647–662.
[47] L.J. Farrugia, J. Appl. Crystallogr. 32 (4) (1999) 837–838.
[48] Bruker AXS, Inc., Madison, WI, USA, 2000.
[49] H.D. Flack, Acta Crystallogr. A39 (1983) 876–881.
[50] Bruker AXS, Inc., Madison, WI, USA, 2009.
[51] A. Coelho, Coelho Software, Brisbane, Australia, 2007.
[52] B.M. Fung, A.K. Khitrin, K. Ermolaev, J. Magn. Reson. 142 (1) (2000) 97–101.
[53] S. Kroeker, J.F. Stebbins, Inorg. Chem. 40 (24) (2001) 6239–6246.
[54] R.K. Harris, E.D. Becker, S.M.C. De Menezes, R. Goodfellow, P. Granger, Pure Appl. Chem. 73 (11) (2001) 1795–1818.
[55] K. Klochko, G.D. Cody, J.A. Tossell, P. Dera, A.J. Kaufman, Geochim. Cosmochim. Acta 73 (7) (2009) 1890–1900.
[56] D. Massiot, F. Fayon, M. Capron, I. King, S. Le Calve, B. Alonso, J.O. Durand, B. Bujoli, Z.H. Gan, G. Hoatson, Magn. Reson. Chem. 40 (1) (2002) 70–76.
[57] Bruker Optik GmbH, Ettlingen, Germany, 2005.
[58] Galactic Industries Corporation, Salem, New Hampshire, 1996.
[59] T. Pettke, in: P. Sylvester (Ed.), Laser ablation ICP–MS in the Earth Sciences: Current Practices and Outstanding issues, Mineral. Assoc. Can. Short Course Series 40 (2008)189–218.
[60] I. Kroslakova, D. Gunther, J. Anal. Atom. Spectrom. 22 (1) (2007) 51–62.
[61] M. Guillong, D.L. Meier, M.M. Allan, C.A. Heinrich, B.W.D. Yardley, in: P. Sylvester (Ed.), Laser ablation ICP–MS in the Earth Sciences: Current Practices and Outstanding Issues, Mineral. Assoc. Can. Short Course Series 40 (2008) 328–333.
[62] N.J.G. Pearce, W.T. Perkins, J.A. Westgate, M.P. Gordon, S.E. Jackson, C.R. Neal, S.P. Chenery, Geostandards Newslett. 21 (1) (1997) 115–144.
[63] T. Armbruster, H.B. Bürgi, M. Kunz, Am. Mineral. 75 (1–2) (1990) 135–140.
[64] N.J. Harrick, Internal Reflection Spectroscopy, Interscience Publishers/Wiley, New York, 1967.
[65] P. Hannaford, R.M. Lowe, Anal. Chem. 49 (12) (1977) 1852–1857.
[66] H. Siebert, Anwendungen der Schwingungsspektroskopie in der anorganischen Chemie, Springer, Berlin, 1966.
[67] V.C. Farmer, The Infrared Spectra of Minerals, Mineralogical Society, London, 1974.
[68] D.C. Harris, B.M.D. Bertolucci, Symmetry and Spectroscopy. An Introduction to Vibrational and Electronic Spectroscopy, Dover, New York, 1989.
[69] N.I. Leonyuk, J. Cryst. Growth 174 (1–4) (1997) 301–307.
[70] H.R. Xia, L.X. Li, J.Y. Wang, W.T. Yu, P. Yang, J. Raman Spectrosc. 30 (1999) 557–561.
[71] M.L. Niven, D.J. Waters, J.M. Moore, Am. Mineral. 76 (1–2) (1991) 246–256.